SOILS AND FOUNDATIONS Vol. 46, No. 4, 491–504, Aug. 2006
Japanese Geotechnical Society

EXPERIMENTAL DETERMINATION OF SOFTENING RELATIONS FOR CEMENT-TREATED SAND

TSUTOMU NAMIKAWA[i] and JUNICHI KOSEKI[ii]

ABSTRACT

Three-point bending tests and plane strain compression tests were conducted to investigate tensile and shear failure in cement-treated sand. The bending test results were used to evaluate the tension fracture energy and crack opening displacements. From these results, the tension-softening relation was obtained using the energy balance approach. In the plane strain compression tests, the strain localization zone that occurs during a strain-softening process and the local displacements across the shear band were identified by an image analysis. The shear-softening relation and the energy consumed during the shear failure were estimated based on these local displacements. After the test, the shear bands that appeared on the specimen surface were observed with a microscope. This microscopic observation revealed the appearance of shear fracture zone and provided information on the thickness of the shear band. Moreover, we discussed the difference in the energies consumed by the tensile failure and the shear failure.

Key words: cement-treated sand, fracture energy, shear failure, strain localization, strain-softening, tensile failure (**IGC**: D6)

INTRODUCTION

Ground improvements by cement-mixing have been applied extensively for structure foundations, excavation control and liquefaction mitigation. To achieve the benefit of the ground improvement, it is necessary to design the improved ground appropriately.

The current design procedure of the improved ground by cement-mixing consists of examinations of the internal and external stabilities. In the analysis of the internal stability, the stresses induced within the cement-treated soil shall not exceed its allowable strength (PWRC, 1999). Therefore, the internal stability often dominates the specifications of the column and wall type improvements in which tensile stresses are easily mobilized by external forces. This design method cannot evaluate appropriately the performance of the ground improvement in the ultimate limit state.

For example, the specification of a lattice-shaped ground improvement for a remediation method against liquefaction is sometimes dominated by the internal stability at high seismic load levels. However, the numerical analysis results suggested that the improved ground can be effective against liquefaction of unimproved ground, even after it partly failed during the earthquake (Namikawa et al., 2005). In such a case, the ground improvement may be designed more rationally by the performance design method in which a partial damage to the improved ground is accepted. The performance design requires an accurate evaluation of the behavior of the ground improvement in which the induced stress exceeds the strength of cement-treated soils. Therefore, to develop an economical and rational design procedure, it is important to investigate the behavior of the cement-treated soils during tensile and shear failures.

During the tensile and shear failures, a strain-softening behavior that accompanies the strain localization phenomenon is observed. The strain localization causes a scale effect, as pointed out by Bažant (1989), among others. It is, therefore, important to determine the stress-strain relationship in the strain localization zone for an accurate evaluation of the post-peak behavior of cement-treated sands.

In relation to the post-peak behavior of stiff geomaterials, Yoshida et al. (1994) conducted a series of plane strain compression tests on dense sands and gravels to obtain the strain-softening relationships in the strain localization zone, i.e. shear band. Siddiquee et al. (1999) simulated the bearing capacity characteristics of stripe footing on sand by FE-analysis in which the strain-softening relationship in shear band was employed. They indicated that the strain-softening characteristics have large effects on the bearing capacity of footing on dense sand, as failure of ground is largely progressive. The deformation properties of shear band obtained by Yoshida et al. (1994) were also used for evaluating the active earth pressures at high seismic load levels (Koseki

[i] Takenaka Corp., Japan (namikawa.tsutomu@takenaka.co.jp).
[ii] Professor, Institute of Industrial Science, University of Tokyo, Japan (koseki@iis.u-tokyo.ac.jp).
The manuscript for this paper was received for review on September 6, 2005; approved on May 29, 2006.
Written discussions on this paper should be submitted before March 1, 2007 to the Japanese Geotechnical Society, 4-38-2, Sengoku, Bunkyo-ku, Tokyo 112-0011, Japan. Upon request the closing date may be extended one month.

et al., 1998). Moreover, the deformation properties of shear band for the rock fill materials were accounted in the modified Newmark method for the seismic design of rock fill dams (Okuyama et al., 2003). The computed results showed that the shear displacement was significantly influenced by the strain-softening relationships which depend on the particle size. These researches suggested that the strain-softening relationship in the strain localization zone is required for evaluating appropriately the performance of soil structure in the ultimate limit state.

Several other experimental studies have also attempted to investigate the shear-softening behavior of geomaterials. In particular, the strain localization of sand has been investigated extensively (Vardoulakis and Goldscheider, 1981; Vardoulakis and Graf, 1985; Han and Drescher, 1993; Finno et al., 1997; Alshibli and Sture, 2000; Desrues and Viggiani, 2004). Moreover, microscopic observations revealed the behavior of sand particles in the shear band (Oda and Kazama, 1998; Oda et al., 2004). Several studies have been also conducted on bonded soils to investigate the shear-softening behavior (Tatsuoka and Kim, 1994; Murata et al., 1995; Hayano et al., 1999; Bhandari and Inoue, 2005). However, for cement-treated soil, the strain-softening relationship in the shear band has not been determined so far.

Three-point bending tests on cement-grouted sand under tensile failure provided the opening crack displacement and the stress intensity factor (Vipulanandan et al., 1994). However, little is known about the tension-softening relation in the bonded soils. Many attempts have been made to determine the tension-softening relation in concrete and mortar (Hillerborg et al., 1976; Bažant and Oh, 1983; Li et al., 1987; Wittmann et al., 1988; Uchida et al., 1991; Niwa et al., 1998). These studies employ the concept of fracture mechanics to determine the tension-softening relation. In this concept, it is assumed that all the energy released during the strain-softening process is consumed for crack opening. The energy released during bond breakage is estimated from the load-displacement relation obtained from the bending or compact tension tests. This estimated energy is used for determining the tension-softening relation.

In view of the above, the purpose of this study is to determine the strain-softening relations for cement-treated sand. Three point bending tests and plane strain compression tests were conducted for studying the tensile and shear failures, respectively. These failure modes were macroscopically defined in this study. The tensile failure was defined as the failure mode caused by excessive tensile stress (i.e., the minor principal stress). In this mode, the failure region would be yielded in the direction that is normal to the minor principal stress. On the other hand, the shear failure was defined as the failure mode caused by excessive shear stress. In this mode, the failure region would incline to the direction of the major principal stress.

The results of bending test were used to evaluate the tension fracture energy and opening crack displacements.

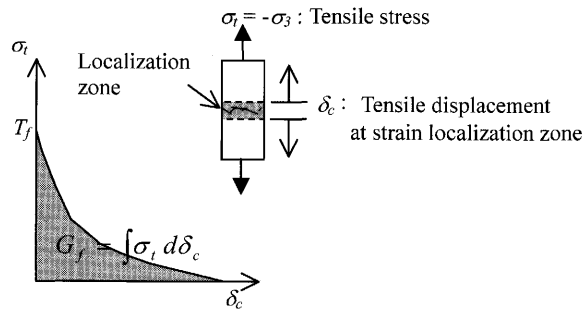

Fig. 1. Schematic tension softening curve and definition of fracture energy G_f

These results were then used to obtain the tension-softening relation by the energy balance approach. In the plane strain compression tests, the strain localization zone that occurs during the strain-softening process and the local displacements across the shear band were identified by an image analysis method. The shear-softening relation and shear fracture energy were estimated using these local displacements. After the test, the shear bands that appeared on the specimen surface were observed with a microscope. This observation revealed an existence of shear fracture zone and provided the thickness of the shear band. Moreover, we discussed the difference in the energies consumed during the tensile and shear failure.

ENERGY BALANCE CONCEPT AND FRACTURE ENERGY

The tensile failure of quasi-brittle materials, such as concrete, rock, and cemented soil exhibits strain localization after the peak tensile strength. The deformation then concentrates inside a narrow band, namely, a strain localization zone. Thus, estimation of the displacement in the strain localization zone is required to determine the post-peak softening relation. Direct tension test is a direct method of determining the softening relation. By assuming the thickness of the localization zone, the external load-displacement relation obtained from the direct tension test can be used to determine the post-peak stress-strain relation in the localization zone. However, there is an inherent problem in this test; it is difficult to maintain a stable condition of loading on the specimen during the softening process.

Therefore, for concrete, methods using the fracture mechanics concept were proposed to determine the post-peak tension-softening relation in a realistic manner (Hillerborg et al., 1976; Bažant and Oh, 1983; Li et al., 1987; Wittmann et al., 1988; Uchida et al., 1991; Niwa et al., 1998). These methods assume that the energy released during the softening process is consumed during the formation and opening of cracks. This assumption implies that the amount of energy released per unit area for widening the cracks corresponds to the area below the tension-softening curve, as shown in Fig. 1 (Hillerborg et al., 1976). The energy consumed per unit crack area is defined as the fracture energy G_f.

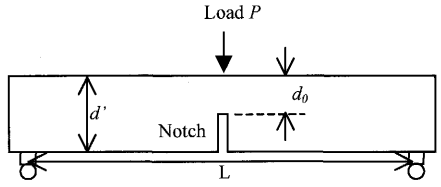

Fig. 2. Three-point bend test on notched beams

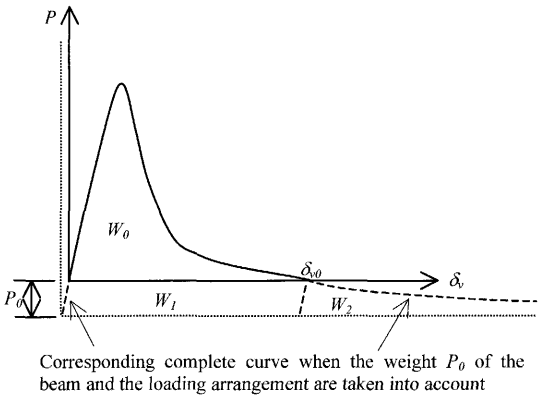

Fig. 3. Schematic load-deflection curve from bending test

The energy released during the softening process must be estimated for calculating G_f. RILEM (Réunion Internationale des Laboratoires et Experts des Matériaux, Systèmes de Constructions et Ouvrages; the International Union of Laboratories and Experts in Construction Materials, Systems and Structures) proposed a method of determining G_f for mortar and concrete by means of a three-point bend tests on notched beams, as shown in Fig. 2 (RILEM, 1985; Hillerborg, 1985). In this method, the load P and the deflection δ_v are measured at the loading point. The $P-\delta_v$ relation is used for estimating G_f. A schematic $P-\delta_v$ curve obtained from the bending test is shown in Fig. 3. The total amount of energy released during the bending test, W_0, is represented by the area below the $P-\delta_v$ curve. However, the self-weight of the beam also contributes the load during the test. Thus, RILEM recommended the consideration of the weight of the beam for calculating G_f. The hypothetical $P-\delta_v$ curve is shown by the dashed lines in Fig. 3. The additional load P_0 is the central load that causes the same central bending moment as the one caused by the weight of the beam. P_0 is expressed as;

$$P_0=\frac{1}{2}mg \tag{1}$$

in which m is the mass of the beam and g is the gravitational acceleration. The total amount of released energy W is defined as;

$$W=W_0+W_1+W_2 \tag{2}$$

W_0 is the area below the measured $P-\delta_v$ curve. W_1 is expressed as;

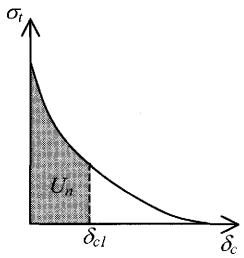

Fig. 4. Energy U_n in Eq. (7)

$$W_1=P_0\delta_{v0}=\frac{1}{2}mg\delta_{v0} \tag{3}$$

where δ_{v0} is the displacement at $P=0$ when the beam breaks completely. The RILEM regulation assumes that W_2 is approximately equal to W_1. Therefore, the total release energy W becomes;

$$W=W_0+2P_0\delta_{v0}=W_0+mg\delta_{v0} \tag{4}$$

This energy when divided by the fractured area A_s gives the fracture energy G_f.

$$G_f=\frac{W}{A_s}=\frac{W_0+mg\delta_{v0}}{A_s} \tag{5}$$

G_f corresponds to the area below the tension-softening curve shown in Fig. 1. The tension-softening relation can be evaluated from G_f, if the shape of the tension-softening curve is known. The evaluation method is described in the next section.

METHOD FOR DETERMINING TENSION-SOFTENING RELATIONS

Several methods have been proposed to determine the tension softening relations for concrete from laboratory test results. Li et al. (1987) proposed a J-integral method based on energy balance. By using two pre-cracked specimens with slightly different notch lengths, they derived the tension-softening curves from the test results. Later, Uchida et al. (1991) modified the J-integral method. Assuming the distribution of the failure process zone width, they developed the tension-softening curve from the results of a test in which single specimen was used. In this study, we estimated the tension-softening relation in cement-treated sand from the bending test results by employing the method proposed by Uchida et al. (1991).

Method Proposed by Uchida et al. (1991)

We consider a relation between tensile stress $\sigma_t=(-\sigma_3)$ and an opening crack displacement δ_c as shown in Fig. 4. σ_t is expressed as;

$$\sigma_t=f(\delta_c) \tag{6}$$

In Fig. 4, the consumed energy per unit crack area U_n at $\delta_c=\delta_{c1}$ can be expressed as;

$$U_n = \int_0^{\delta_{c1}} f(\delta_c) d\delta_c \tag{7}$$

Next, we consider the energy consumed in a failure process zone. A schematic illustration of the failure process zone in the bending test on a notched specimen is shown in Fig. 5(a). In this case, the total energy consumed in the failure process zone, U, can be expressed as;

$$U = B_b \int_0^d U_n(\delta_c(x)) dx \tag{8}$$

in which B_b is the width of the beam. After determining the consumed energy U, the length of the failure process zone, d, and the opening crack displacement $\delta_c(x)$ from the bending test, the differentiation of Eq. (8) with respect to δ_c provides U_n. The subsequent differentiation of Eq. (7) provides σ_t as a function of δ_c.

This method requires the relationships between U and $\delta_c(x)$ to determine the $\sigma_t - \delta_c$ relation. In order to obtain the $\sigma_t - \delta_c$ relation from the bending test results, Uchida et al. (1991) made two assumptions: (a) The external energy applied to a specimen is completely consumed in the failure process zone, and (b) the failure process zone propagates throughout the ligament portion immediately after loading, and $\delta_c(x)$ varies linearly along the failure process zone. Assumption (a) implies that U is defined by the area below the $P - \delta_v$ curve, as shown in Fig. 6.

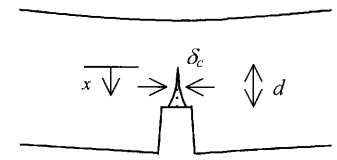

d: Length of a failure process zone
δ_c: Opening crack displacement

(a)

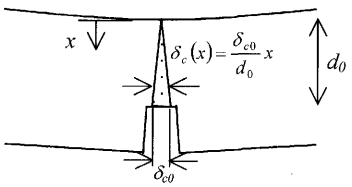

δ_{c0}: Opening crack mouth displacement

(b)

Fig. 5. Failure process zone: (a) General failure process zone and (b) Failure process zone assumed by Uchida et al. (1991)

Assumption (b) implies that $\delta_c(x)$ is distributed as shown in Fig. 5(b). Here, $\delta_c(x)$ is expressed as;

$$\delta_c(x) = \frac{\delta_{c0}}{d_0} x \tag{9}$$

in which δ_{c0} is the opening crack mouth displacement. Changing variables from x to δ_c in Eq. (8), the following equation is obtained.

$$U(\delta_{c0}) = \frac{B_b d_0}{\delta_{c0}} \int_0^{\delta_{c0}} U_n(\delta_c) d\delta_c = \frac{A_{lig}}{\delta_{c0}} \int_0^{\delta_{c0}} U_n(\delta_c) d\delta_c \tag{10}$$

in which A_{lig} is the area of the ligament of the beam. The second order differentiation of U with respect to δ_{c0} gives the following equations.

$$U'(\delta_{c0}) = -\frac{A_{lig}}{\delta_{c0}^2} \int_0^{\delta_{c0}} U_n(\delta_c) d\delta_c + \frac{A_{lig}}{\delta_{c0}} U_n(\delta_{c0})$$

$$= -\frac{U(\delta_{c0})}{\delta_{c0}} + \frac{A_{liq}}{\delta_{c0}} U_n(\delta_{c0})$$

$$U_n(\delta_{c0}) = \frac{1}{A_{lig}} \{U(\delta_{c0}) + \delta_{c0} U'(\delta_{c0})\}$$

$$\sigma_t = U_n'(\delta_{c0}) = \frac{1}{A_{lig}} \{2U'(\delta_{c0}) + \delta_{c0} U''(\delta_{c0})\} \tag{11}$$

After measuring U and δ_{c0} in the bending test, the value of σ_t corresponding to δ_{c0} can be calculated using Eq. (11). By employing this method, σ_t was estimated from the bending test results in the following sections.

THREE-POINT BENDING TEST

Experimental Program

The three-point bending tests were conducted to determine the tension-softening curve for cement-treated sand. Three specimens shown in Table 1 were tested. Based on the RILEM regulation, a beam specimen with a central notch was used in the tests (*see* Fig. 2). The notch

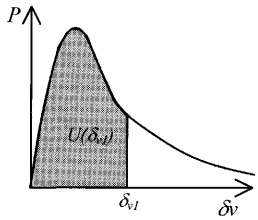

Fig. 6. Energy defined from load-deflection ($P - \delta_v$) curve

Table 1. Summary of three point bending tests

Case	Curing time (hour)	Width B_b (mm)	Depth d' (mm)	Length (mm)	Span length L (mm)	Effective depth d_0 (mm)	Notch size (mm)	Dry density (g/cm^3)	Water content (%)
BAb-1	167	40.9	40.1	179.6	160	20.0	20.1	1.59	20.6
BAb-2	164	39.2	39.6	179.2	160	19.9	19.7	1.59	20.0
BAb-3	166	40.2	40.0	180.8	160	20.1	19.9	1.61	19.9

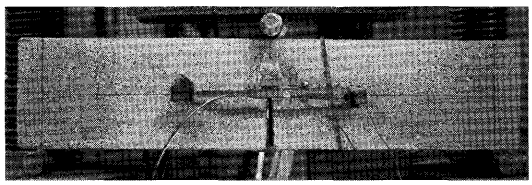

Fig. 7. Specimen for three point bending test

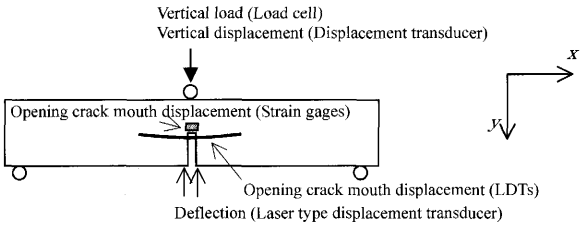

Fig. 8. Measurement items in three point bending test

Table 2. Mixing proportions of cement-treated sand

Materials	Toyoura sand	Portland cement	Bentonite	Water
Weight (%)	66.3	10.0	5.0	18.7

depth was equal to half the beam depth. A photograph of the specimen under loading is shown in Fig. 7. As shown in Fig. 8, the load, the deflections at the center of the beam, and the opening crack mouth displacements were measured during the loading process. The deflections were measured at the center of the beam by laser-type displacement transducers. The opening crack mouth displacements were measured at both sides of the beam by local displacement transducers (LDTs), *see* Goto et al. (1991) for the details of LDTs.

The composition of the cement-treated sand used in the tests is described in Table 2. The specimen was made by compaction after mixing thoroughly all the materials that composed the cement-treated sand. The mold used for preparing the specimens was 23 cm in height with an inner cross section of 6×8 cm. The specimen was compacted in the x direction as defined in Fig. 8. The curing time was 7 days. The target strength was approximately 1800 kPa in unconfined compression tests (Namikawa, 2006). After curing, the specimens were trimmed to the prescribed size and notched with a saw. The width of the notch was 2.5 mm. During the test, vertical loading rate of 0.01 mm/min was maintained.

Experimental Results

The load-deflection ($P-\delta_v$) curves of the three specimens are shown in Fig. 9(a). The $P-\delta_v$ relations are repeatable even after the peak loads, thereby indicating the existence of a unique strain-softening relation of the cement-treated sand. The tension fracture energy calculated from these $P-\delta_v$ curves is shown in Table 3. The resulting fracture energy G_f ranged from 9 to 12 N/m. The relationships between the load P and the opening crack mouth displacement δ_{c0} are shown in Fig. 9(b). The $P-\delta_{c0}$ relations are also repeatable after the peak load. At the complete failure at $P=0$, the value of δ_{c0} reached approximately 0.3 mm.

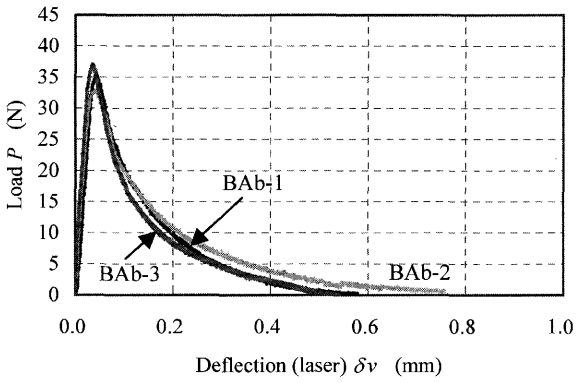

(a)

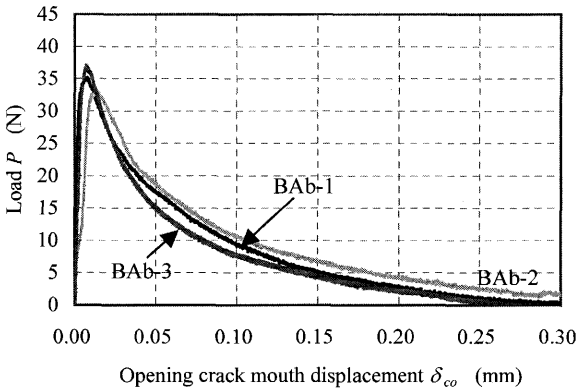

(b)

Fig. 9. Bending test results: (a) Load-deflection curves and (b) Load-opening crack mouth displacement curves

Table 3. Fracture energy G_f obtained from bending tests

Case	P_{max} (N)	W_0 (N·m)	W (N·m)	G_f (N/m)
BAb-1	35	0.0050	0.0078	9.6
BAb-2	33	0.0059	0.0094	12
BAb-3	37	0.0049	0.0075	9.3

Relationships between Stress and Opening Crack Displacement ($\sigma_t-\delta_c$ Relations)

The $\sigma_t-\delta_c$ relations were estimated from the bending test results. The consumed energy U corresponding to δ_{v1} is defined as the area below the load-deflection curve as shown in Fig. 6. The second order differentiation of U with respect to δ_{c0} yields the relationship between σ_t and δ_c. The normalized $\sigma_t-\delta_c$ relations calculated by Eq. (11) are shown in Fig. 10. A tensile strength T_f of 0.38 N/mm^2, which was obtained from the direct tension tests (Koseki et al., 2005b), was assumed and the values of G_f shown in Table 3 were used here. There are no significant differences in the three $\sigma_t-\delta_c$ curves. The 1/4 bilinear

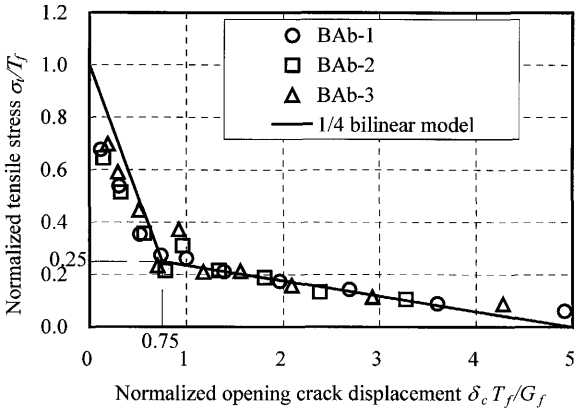

Fig. 10. Tension softening relations

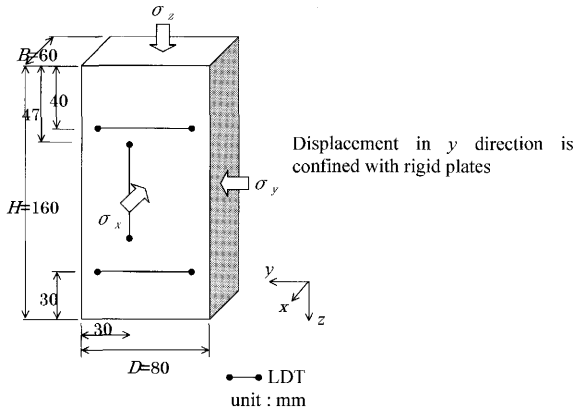

Fig. 11. Configuration of plane strain compression specimen

model developed for concrete is also shown in this figure (Rokugo et al., 1989). With the model, the break point is located at $\delta_c T_f/G_f=0.75$ and $\sigma_t/T_f=0.25$. These results show that the 1/4 bilinear model can properly express the tension-softening relations of the cement-treated sand.

PLANE STRAIN COMPRESSION TEST

Experimental Program

The plane strain compression tests were conducted to obtain the shear-softening curve for the cement-treated sand. The test configuration and definition of coordinates are shown in Fig. 11. The composition of the cement-treated sand used for the tests is the same as that used for the bending tests (*see* Table 2). The specimen was made by compaction after mixing the materials thoroughly. The mold used for preparing the specimens was 23 cm in height with an inner cross section of 6×8 cm. The curing time was 7 days. The specimen was then trimmed at both ends to a height of 16 cm and set in the pressure cell. After the specimen was saturated by a double vacuuming method (Ampadu and Tatsuoka, 1993), it was isotropically consolidated to the prescribed confining stress of 49 kPa or 88 kPa. Then the cell pressure and the backpressure were decreased simultaneously, while maintaining the same effective stress state. Thus, by using a partial vacuum as the backpressure, the cell pressure was released to zero, and the pressure cell could be removed. The confining plates were contacted with the specimen and a stress of approximately 560 kPa in the y direction was applied to achieve a sufficient contact between them. Under drained condition, compression stress was applied in the z direction at a constant strain rate of 0.01%/min. More details on the test apparatus are available in literature (Koseki et al., 2005a).

The loads in the y and z directions were measured by an inner load cell that is free from the effects of friction at the bearing. The displacement of the loading shaft was measured by an external displacement transducer. The strain measured by this transducer is herein denoted as ε(external). The displacements of the specimen surface were also measured by local displacement transducers (LDTs). The strain measured by these transducers (LDTs) is denoted as ε(LDTs).

The local deformation properties at the specimen surface normal to the y direction were evaluated by an image analysis method. A latex membrane whose surface was imprinted with a grid of points spaced 5 mm apart was used in the tests. Digital photographs of the surface were taken during the test through a transparent confining plate. After the test, the coordinates of each point were read from the photographs recorded at different loading stages using an image tracking program. The strain components of four-node rectangular elements were calculated from the displacement of each point using linear interpolation functions. The accuracy of the measured displacements is in the order of 0.01 mm (Namikawa, 2006).

The test conditions are summarized in Table 4. A total of 9 tests were performed at $\sigma_x=49$ kPa and 88 kPa. In all the tests except for Pc-4, both the top and bottom ends of the specimen were lubricated with a layer of silicon grease and a 0.3 mm-thick membrane. In test Pc-4, gypsum slurry was poured between the specimen and the membrane to ensure uniform stress and strain distribution (Murata et al., 1995). During the strain-softening process in tests Pb-4 and Pc-5, the specimen was unloaded at the residual stress ratio R_s of 0.8 to observe the failure zone with a microscope. The residual stress ratio R_s is defined as;

$$R_s=\frac{q_{1\max}-q_1}{q_{1\max}-q_{1\text{residual}}} \qquad q_1=\sigma_z-\sigma_x \tag{12}$$

in which $q_{1\max}$ is the peak deviator stress and $q_{1\text{residual}}$ is the residual deviator stress (Yoshida et al., 1994).

More details on the above testing method are available in literature (Salas-Monge, 2002; Salas-Monge et al., 2003).

Experimental Results

The relationships between the deviator stress q_1 and the strain ε_z for tests Pc-1 and Pc-3 are shown in Fig. 12. Both tests exhibited similar stress-strain relationships. The large differences between ε_z(external) and ε_z(LDTs) during the initial loading stage are due primarily to the

Table 4. Summary of plane strain compression tests

Case	Curing time (hour)	σ_x (kPa)	Dry density (g/cm^3)	Water content (%)	q_{1max} (kPa)	b value at q_{1max}	Specimen end	Unload during softening process
Pb-1	168	49	1.59	22.2	1800	0.25	L	No
Pb-2	168		1.59	22.6	1990	0.24	L	No
Pb-3	168		1.60	24.8	2010	0.25	L	No
Pb-4	164		1.59	22.5	1990	0.23	L	Yes
Pc-1	165	88	1.59	23.3	2200	0.20	L	No
Pc-2	167		1.60	22.1	2080	0.24	L	No
Pc-3	167		1.60	22.6	2280	0.20	L	No
Pc-4	167		1.60	22.7	2410	0.25	L+C	No
Pc-5	168		1.61	22.2	2340	0.24	L	Yes

q_{1max}: Peak value of $\sigma_z-\sigma_x$, b value: $(\sigma_y-\sigma_x)/(\sigma_z-\sigma_x)$ at q_{1max}, L: Lubrication, L+C: Lubrication+Capping with gypsum

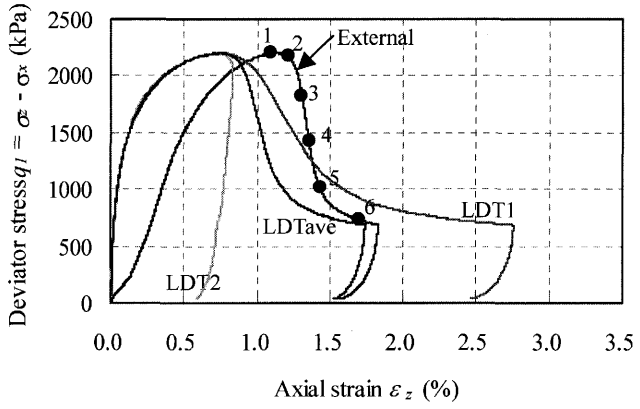

(a)

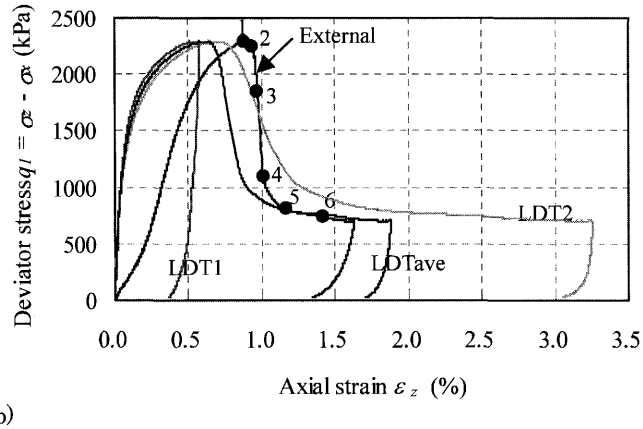

(b)

Fig. 12. Stress-strain relations in plane strain compression tests: (a) Test Pc-1 and (b) Test Pc-3

effect of bedding error. Both the specimens exhibited the strain-softening behavior after the peak strength. During the strain-softening process, the readings for LDT1 and LDT2 that were attached on the opposite ends varied drastically in both tests. These variations are due to their dissimilar positions relative to the failure zone. The specimen after test Pc-1 is shown in Fig. 13. A failure

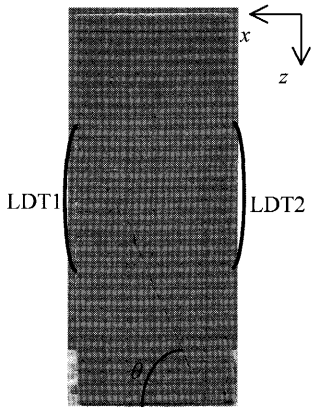

Fig. 13. Shear band formed in Pc-1

crack appeared in the direction from the bottom right to the left of the specimen. Thus, the strain across the crack measured with LDT1 increased at a large rate after the peak strength, whereas the strain measured with LDT2 decreased, thereby indicating rebound deformation in Fig. 12(a).

The maximum shear strain $\gamma_{max}(=\varepsilon_1-\varepsilon_3)$ distributions of specimens in tests Pc-1 and Pc-3 obtained from the image analysis method are shown in Fig. 14. The figure numbers correspond to the respective strain-softening stages as shown in Fig. 12. In test Pc-1, strain localization began at the peak stress state. Two failure zones developed during the strain softening process. The first failure zone appeared in the direction from the bottom left to the right of the specimen. Thereafter, development of the first failure zone stopped and the second failure zone, which eventually dominated the failure behavior of the specimen, developed at the location on the specimen where the crack was observed after the test (*see* Fig. 13). The first and second failure zones lie along conjugate, i.e. the two directions are almost symmetrically reflected about the vertical. Similarly, in test Pc-3, strain localization began at the peak stress state. However, a single

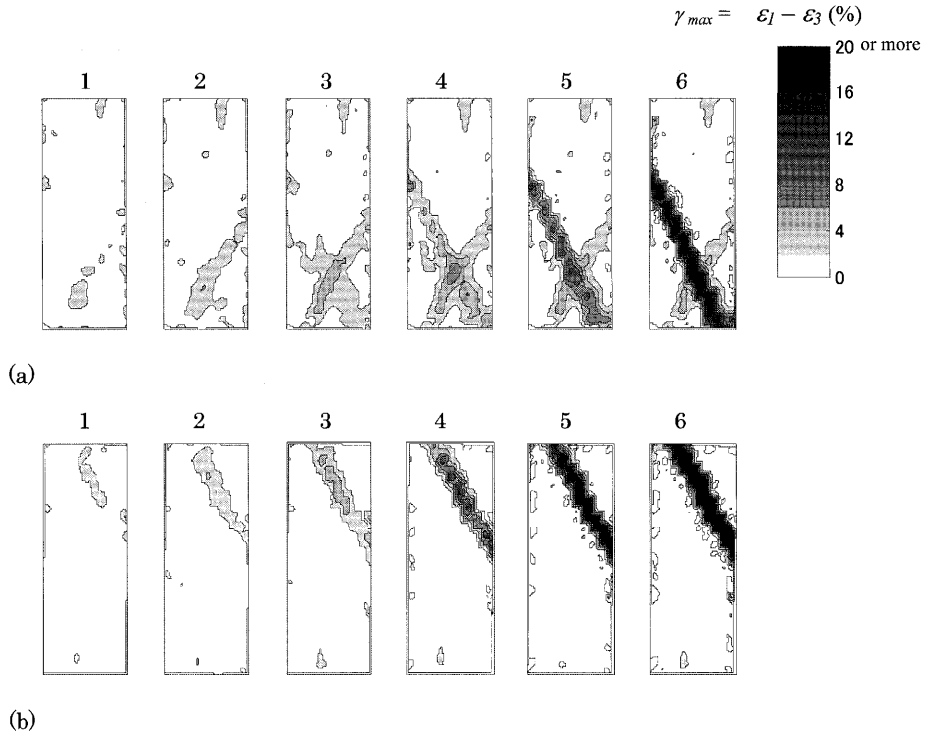

Fig. 14. Evolution of strain localization zone in tests: (a) Test Pc-1 and (b) Test Pc-3

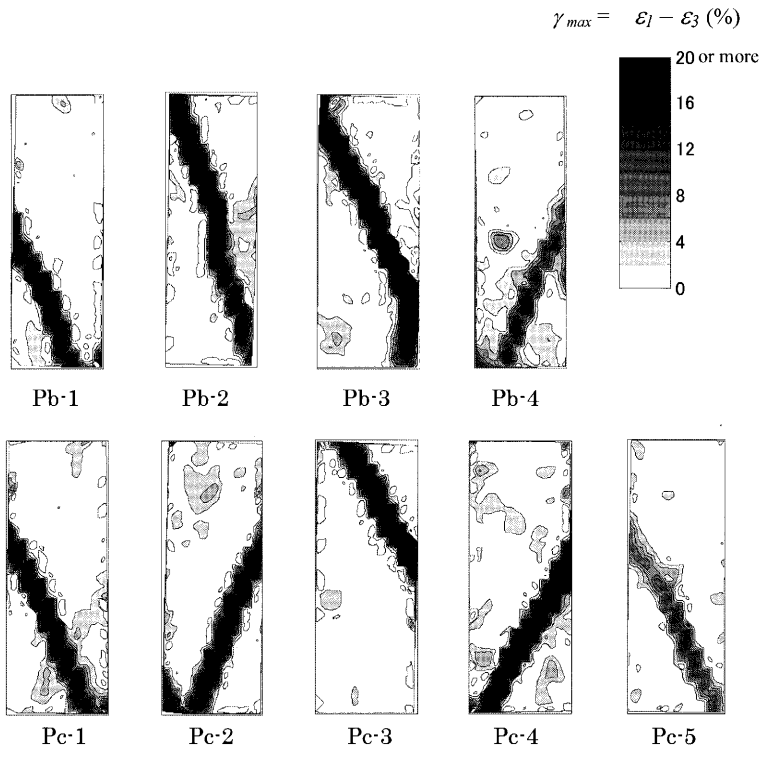

Fig. 15. Distributions of maximum shear strain at residual stress state

persistent failure zone developed during the softening process. These image analysis results demonstrate the complexity of strain localization patterns. Although the other tests were also performed under similar conditions, different strain localization patterns were observed during shear failures. These results indicate that it is required to estimate the local displacement across the failure zone for accurately estimating the strain in the failure zone.

The strain localization patterns in all the tests are shown in Fig. 15. It is observed that the localization zone comprises both inclined and vertical zones in tests Pb-2 and Pb-3 that were performed at $\sigma_x = 49$ kPa. The vertical

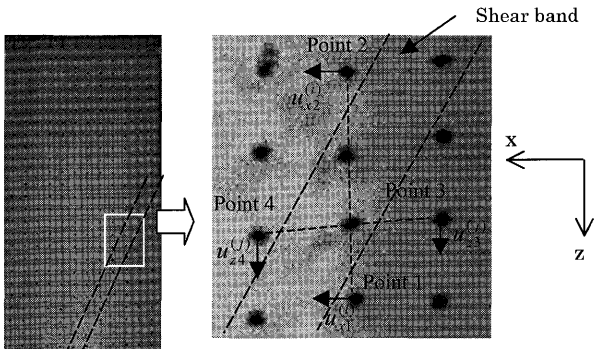

$u_{x1}^{(i)}$: Displacement in x direction at point 1
$u_{x2}^{(i)}$: Displacement in x direction at point 2
$u_{z3}^{(j)}$: Displacement in z direction at point 3
$u_{z4}^{(j)}$: Displacement in z direction at point 4

Local displacement : $u_x^{(i)} = u_{x2}^{(i)} - u_{x1}^{(i)}$, $u_z^{(j)} = u_{z4}^{(j)} - u_{z3}^{(j)}$

$$u_x = \frac{\sum_{i=1}^{m} u_x^{(i)}}{m} \qquad u_z = \frac{\sum_{j=1}^{n} u_z^{(j)}}{n}$$

m,n : The number of measurement points

Fig. 16. Evaluation method of displacement across shear band from image analysis results

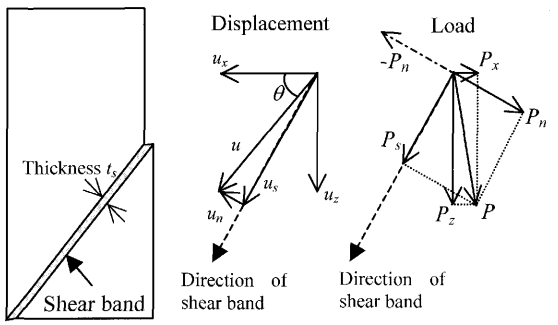

Fig. 17. Method to obtain relative displacement across shear band (Yoshida et al., 1994)

Table 5. Energy consumed per unit shear band area G_{fs}

Case	θ (degree)	W_s (N·m)	G_{fs} (N/m)
Pb-1	65	1.1	100
Pb-4	66	—	—
Pc-1	64	1.8	160
Pc-2	66	1.6	140
Pc-3	62	1.9	180
Pc-4	64	2.0	180
Pc-5	63	—	—

localization zone can be identified as the splitting tensile failure zone. In cement-treated soils, a splitting tensile failure is known to occur during the compression tests conducted at low confining stresses (Kobayashi and Tatsuoka, 1982). The strain-softening relation for the test results that include the splitting tensile failure may differ from that for the results in which only shear failure occurs. Thus, we did not use the results of tests Pb-2 and Pb-3 for determining the strain-softening relation in the failure zone in the following section. Although further investigation is required to clarify the fracture mechanism of the splitting tensile failure under compression, this issue is beyond the scope of this study.

Deformation of the Failure Zone

Yoshida et al. (1994) estimated the local displacement across a shear band of sand from the relative displacement of the points of a grid printed on a membrane. By employing similar procedures, the deformations of the failure zone were estimated from the image analysis results. As shown in Fig. 16, the relative vertical displacements between two points on both sides of the single failure zone that appeared finally were evaluated. The horizontal relative displacements across the failure zone were also evaluated in the same manner. The values of the vertical relative displacement u_z and the horizontal relative displacement u_x for an entire failure zone were obtained by averaging these local displacements. The combination of the components u_z and u_x gives the local relative displacement vector u across the failure zone (*see* Fig. 17). Based on the observed inclination of the failure zone, the sliding displacement u_s across it and the change in the failure zone thickness u_n can be calculated from u (*see* Fig. 17). In this experiment, the inclination of the failure zone was determined from that of the crack observed on the specimen after the test (*see* Fig. 13). The estimated inclination of the failure zone, θ, is listed in Table 5.

The relationships between the load P_z measured in the z direction and the increment in the sliding displacement from the peak stress state, $u_s - u_{s\,peak}$, are shown in Fig. 18(a). Although slight differences were observed in the peak loads, there were no significant differences in the load-local displacement relationships in all the tests. The relationships between the $u_s - u_{s\,peak}$ and the increment of the failure zone thickness from the peak stress state, $u_n - u_{n\,peak}$, are shown in Fig. 18(b). The value of $u_n - u_{n\,peak}$ increases in proportion to $u_s - u_{s\,peak}$ in all the tests, thereby indicating that the rate of dilation in the failure zone does not change considerably during the softening process.

Microscopic Investigation

The failure zones on the specimen surface were observed with a microscope after the tests. The failure zones observed in specimens Pb-1 and Pb-4 are shown in Fig. 19. As mentioned above, the specimen Pb-4 was unloaded in the course of the softening process. The shear band formed during the softening process could be observed on the surface of the specimen Pb-4, while the shear band was widened to a complete crack in the specimen Pb-1 after complete strain softening. In the shear band, it was observed that the bonds of the sand particles were broken in all directions.

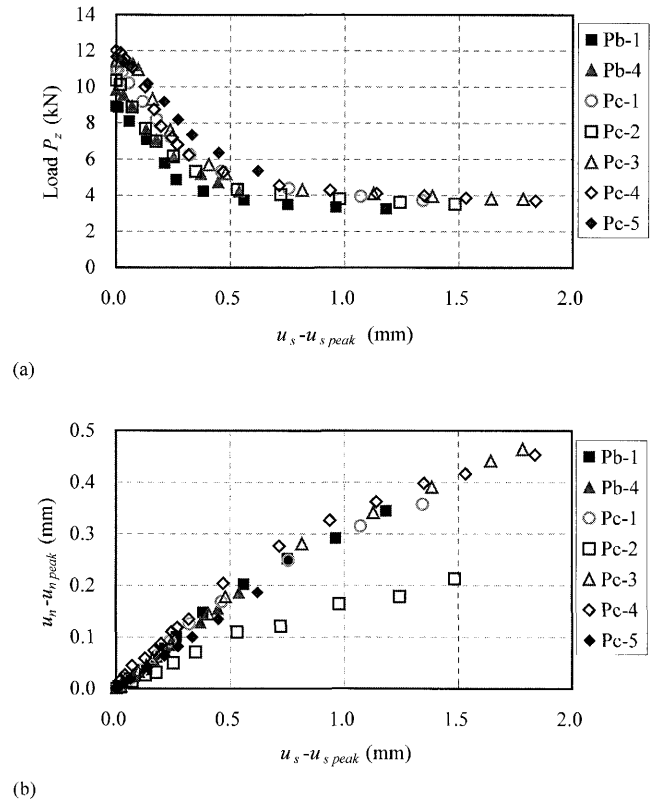

Fig. 18. Deformations of failure zone: (a) Relationships between load and $u_s - u_{s\,peak}$ and (b) Relationships between $u_s - u_{s\,peak}$ and $u_n - u_{n\,peak}$

The thickness of the shear band formed on the specimen surface was measured after tests Pb-1, Pc-1 and Pc-2. The average thickness of the shear band observed after the tests was approximately 0.9 mm. Figure 18(b) shows that the failure zone thickness increases by approximately 0.3 mm during the softening process. Thus, the initial thickness of the shear band, t_s, is roughly estimated to be 0.6 mm. This value is approximately 3 times the mean particle size of Toyoura sand that constitutes the cement-treated sand. The ratio of the shear band thickness to the mean grain size for Toyoura sand is reported to be within the range 10–15 (Oda et al., 2004). The difference in the shear band thicknesses of Toyoura sand with/without cement-treatment may be due to the effect of cementation, since cementation of the treated sand would restrict the movement of the sand particles along the shear band boundary, resulting into narrower shear band than that without cementation.

It is noted that there is a technical difficulty in the determination of shear band thickness. Oda and Kazama (1998) pointed out that the *X*-ray image of the shear band changes in its shape and thickness from section to section. In this study, the thickness of the shear band was measured on the surface of the specimen, which may be somewhat different from the ones inside of the specimen.

Stress-strain Relationships in the Failure Zone

The strain in the failure zone during the shear-softening process was estimated from u_s and u_n. Two strain components, i.e., the shear strain γ and the normal strain in the direction perpendicular to the shear band ε_n, were calculated. They are defined as

$$\gamma = \frac{u_s}{t_s}, \quad \varepsilon_n = -\frac{u_n}{t_s} \tag{13}$$

Assuming the other normal strain component that is parallel to the shear band to be negligible, the invariant of deviator strain, $\bar{\varepsilon} = \sqrt{1/2 \varepsilon_{ij}^s \varepsilon_{ij}^s}$ (ε_{ij}^s: deviator strain), and volumetric strain v were calculated from γ and ε_n.

The stress-strain relationships in the persistent failure zone are shown in Fig. 20(a). It should be noted that there may be variations in normal stresses from outside to inside the shear band in the plane of the shear band (Lade, 2003). However, since it is difficult to measure the stress in the shear band, the second invariant of the deviator stress J_2 that is evaluated globally and normalized by its peak value is employed in the present study. In addition, based on the microscopic observation as mentioned above, the thickness of the shear band t_s is assumed to be 0.6 mm. Since there are no significant differences in the stress-strain relationships for all the tests, the softening relation may not be influenced significantly by the confining pressure. This suggests that a unique curve can be determined to describe the shear-softening relationship in the persistent failure zone. An exponential function that was proposed originally for expressing the strain-softening relations in sands (Siddiquee et al., 1999) was modified and used in the present study for expressing the strain-softening relations in the cement-treated sand.

$$\sqrt{J_2} = \sqrt{J_{2\,\mathrm{residual}}} + (\sqrt{J_{2\,\mathrm{peak}}} - \sqrt{J_{2\,\mathrm{residual}}}) \exp\left(-\frac{\bar{\varepsilon} - \bar{\varepsilon}_{\mathrm{peak}}}{e_r}\right) \tag{14}$$

is which $J_{2\,\mathrm{peak}}$ is the second invariant of the deviator stress at the peak stress state, $J_{2\,\mathrm{residual}}$ is the residual second invariant of the deviator stress and e_r is a material parameter. When the residual stress ratio $\sqrt{J_{2\,\mathrm{residual}}}/\sqrt{J_{2\,\mathrm{peak}}}$ is set at 0.25, the value of e_r determined by the test

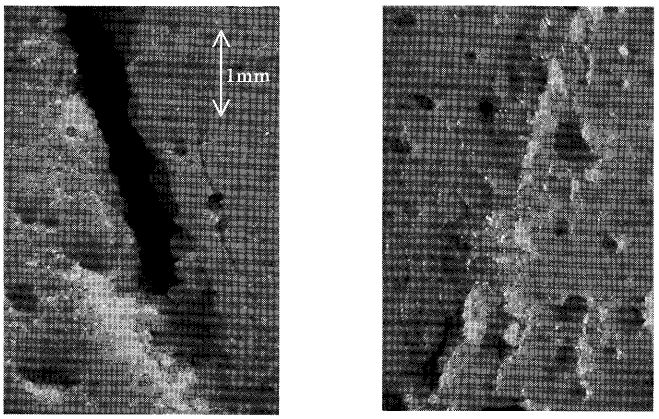

Fig. 19. Failure zone on the specimen surface in plane strain compression tests: (a) Test Pb-1 and (b) Test Pb-4

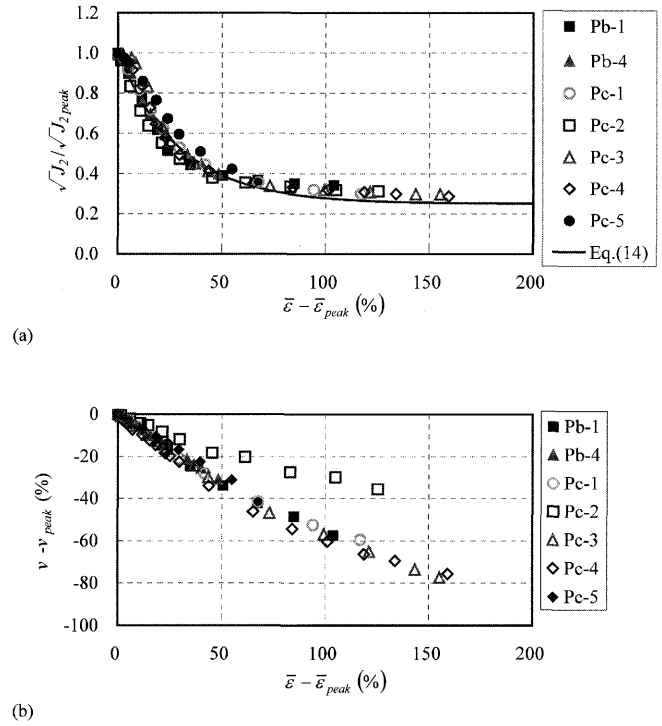

Fig. 20. Stress-strain relationships in failure zone: (a) Relationships between normalized invariant of deviator stress, $\sqrt{J_2}/\sqrt{J_{2\,peak}}$, and increment of invariant of deviator strain, $\bar{\varepsilon}-\bar{\varepsilon}_{peak}$, in shear band and (b) Relationships between increment of invariant of deviator strain, $\bar{\varepsilon}-\bar{\varepsilon}_{peak}$, and increment of volumetric strain, $v-v_{peak}$, in shear band

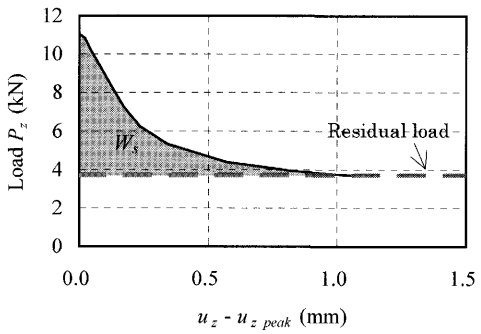

Fig. 21. Energy W_s consumed during shear softening process

results is 0.3. This approximate curve is also shown in Fig. 20(a). As shown in this figure, the approximate curve could describe reasonably the strain-softening relations of the cement-treated sand.

The relationships between $\bar{\varepsilon}-\bar{\varepsilon}_{peak}$ and $v-v_{peak}$ in the failure zone are shown in Fig. 20(b). In all the tests, the value of $v-v_{peak}$ decreases proportionally with an increase in $\bar{\varepsilon}-\bar{\varepsilon}_{peak}$. The ratios of $v-v_{peak}$ to $\bar{\varepsilon}-\bar{\varepsilon}_{peak}$ range from -0.3 to -0.6.

Energy Consumed for Breakage of Cementation during Shear Failure

The energy consumed for breaking cementations in the shear band, W_s, was estimated from the image analysis results. W_s is defined as the area between the softening load-displacement curve and the residual load level (*see* Fig. 21). It is assumed that the area below the residual load level represents the energy dissipated by friction. The same interpretation was suggested regarding the energy surplus in the progressive failure process of overconsolidated clay (Palmer and Rice, 1973). In computing W_s, the relationships between the vertical displacement across the shear band, u_z, and the vertical load P_z were used, while considering the effects of energy dissipation by dilation.

The energy that is dissipated by the shear deformation of the shear band is defined as the product of the sliding displacement increment Δu_s and the load component parallel to the shear band, P_s (*see* Fig. 17). This shear deformation induces the dilation as well (Taylor, 1948). The energy supplied for the dilation is evaluated as the product of the shear band thickness increment Δu_n and the reacting load component normal to the shear band, $-P_n$. Therefore, the amount of energy consumed for the friction and the breakage of cementation can be expressed as $P_s\Delta u_s+P_n\Delta u_n$ $(=P_s\Delta u_s-(-P_n\Delta u_n))$. The value of $P_s\Delta u_s+P_n\Delta u_n$, corresponds to the product of the applied force P and the displacement increments across the shear band, Δu. Since there is no change in the horizontal force P_x, W_s is consequently evaluated from the relationship between the vertical force P_z and displacement u_z, as shown in Fig. 21.

The energy consumed per unit shear band area, G_{fs}, was calculated by the following equation.

$$G_{fs}=\frac{W_s\cos\theta}{BD} \tag{15}$$

in which B is the specimen width and D is the specimen depth (*see* Fig. 11). θ was determined from the angle of the crack observed on the specimen after the test (*see* Fig. 13). The values of G_{fs} are listed in Table 5, which range from 100 N/m to 180 N/m. G_{fs} was considerably larger than G_f obtained during the tensile failure (*see* Table 3). The reason for the difference in energies consumed by the shear failure and the tensile failure will be discussed in the following section.

COMPARISON BETWEEN ENERGIES CONSUMED BY TENSION AND SHEAR FAILURES

We discussed the tensile and shear failures on the macro scale in the previous sections. The relationship between the tensile and shear failure energies is examined on the micro scale in this section. Bažant and Xiang (1997) proposed that the compression failure of concrete can be modeled as the propagation of a band of tensile microcracks. They explained the compression failure mechanism by the energy balance condition, stating that the energy released for the crack band formation is equal to the energy consumed by the formation of tensile splitting microcracks. Similarly, if we assume both of the tensile and shear failures are linked to tensile microcracks in the opening crack mode, the shear-softening and tension-softening relations may also be related to each

other. Thus, it may be possible to estimate both of them based on single test result. In this section we also discuss the relationship between the energy consumed by the shear failure and the tensile failure using an idealized model employing the above assumption.

The average fracture energy for the tensile failure, G_f, is approximately 10 N/m (*see* Table 3), whereas that for the shear failure, G_{fs}, is approximately 150 N/m (*see* Table 5). The ratio of G_f to G_{fs} is approximately 1:15. This significant difference may be attributed to the difference in the cementation areas that are broken in the failure zone. The tensile crack at the tip of the notch is shown in Fig. 22. This photograph was taken with the microscope during the softening process in the bending test (Namikawa and Koseki, 2005). A line crack was formed during tensile failure in the direction normal to the applied tensile stress. In contrast, the failure zone formed during shear failure is the shear band whose thickness is 0.9 mm at the residual stress state (*see* Fig. 19). In the shear band as mentioned before, the bonds between the sand particles are broken in all directions. These microscopic observations indicate that the breakage area of cementation in the shear failure is considerably larger than that in the tensile failure.

We assume herein that the breakage area of cementation can be represented by the number of separated bonds between the sand particles that constitute the cement-treated sand. In addition, the sand particles are simplified into monosized spheres. They are arranged according to two idealized packing geometries, a simple cubic lattice and a face-centered cubic lattice (*see* Fig. 23). First, we consider a case with the simple cubic lattice packing in which the failure zones develop normal to the direction A as defined in the figure. The breakage contacts for the unit column of the tensile and shear failure zones are shown in Fig. 24. With this packing, the total number of contacts N_c for a single particle is 6. During the tensile failure, the number of contacts N_{ct} suffering the breakage of cementation is equal to 1 for a single particle. On the other hand, the number of the breakage contacts N_{cs} for the unit column across the shear band during the shear failure is expressed as,

$$N_{cs} = \frac{N_c}{2} N_p + N_{ct} \tag{16}$$

in which N_p is the number of particle layers in the shear band. As mentioned above, the ratio of shear band thickness to the particle diameter is observed to be 3. Therefore, N_p is set equal to 3, and the substitution of this value in Eq. (16) yields $N_{cs} = 10$ with this packing. From $N_{ct} = 1$ and $N_{cs} = 10$, the ratio of breakage contacts, $R_b = N_{cs}/N_{ct}$, is evaluated to be 10.

The values of R_b for other failure patterns were evaluated in the same manner (*see* Table 6). They are within the range of 6 to 10. Consequently, although R_b is smaller than the ratio of the fracture energy, G_{fs}/G_f, the difference between G_{fs} and G_f can be explained partially by the difference in the area of cementation breakage.

The difference between R_b and G_{fs}/G_f may be partly attributed to the difference in the energies consumed per

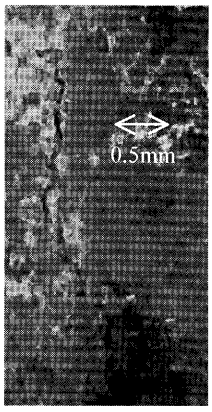

Fig. 22. Failure zone caused by tensile stress in bending test (Namikawa and Koseki, 2005)

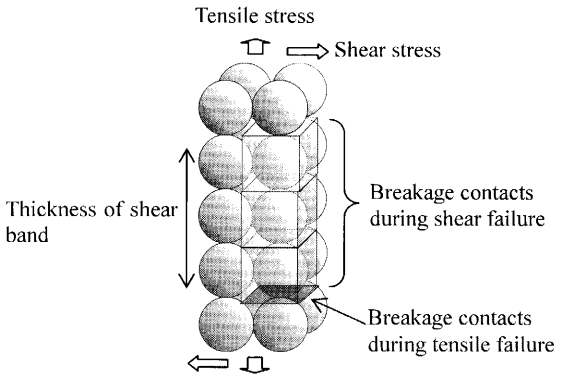

Fig. 24. Breakage contacts per unit column in condition of simple cubic lattice packing

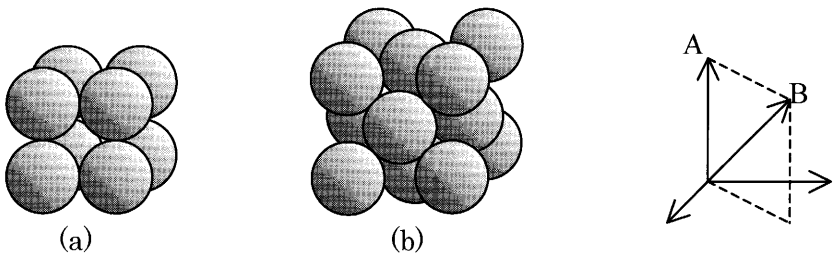

Fig. 23. Idealized grain geometries for uniform spheres in packing order of: (a) simple cubic lattice and (b) face-centered cubic lattice

Table 6. Number of breakage contacts in failure zone

	Direction	N_p	N_c	N_{ct}	N_{cs}	R_b
Simple cubic lattice	A	3.0	6	1	10	10
	B	5.2	6	3	19	6.2
Face-centered cubic lattice	A	4.2	12	4	29	7.3
	B	3.7	12	3	25	8.4

N_p: Number of particle layers in shear band, N_c: Number of contacts for one particle, N_{ct}: Number of breakage contacts per unit column during tensile failure, N_{cs}: Number of breakage contacts per unit column during shear failure, R_b: N_{cs}/N_{ct}

unit breakage area that depend on the microscopic fracture modes. In the above discussion, we assumed that the macroscopic shear failure region consists of tensile microcracks induced in the opening crack mode. However, the shear microcracks induced in the sliding crack mode may rather be yielded in the shear failure region, or possibly, the mixed mode of microscopic fracture occurs in the shear band. Thus, the above difference between R_b and G_{fs}/G_f implies that the energy consumed per unit breakage area for the shear microcrack is larger than that for the tensile microcrack. Further studies on the micro scale are required to clarify the microscopic fracture mode in the shear band.

The accuracy of measurement of the shear band thickness may also cause the difference between R_b and G_{fs}/G_f. As mentioned before, the thickness of the shear band was measured on the surface of the specimens in this study. The observation of the shear band inside of the specimen might enable better understanding about the relationship between G_{fs} and G_f.

The plane strain compression test with the image analysis to obtain the G_{fs} values quantitatively requires sophisticated test equipments and techniques, whereas the bending test to obtain the G_f values is relatively simple. If the relation between G_{fs} and G_f is clarified, the value of G_{fs}, which characterizes the shear-softening behavior, can be obtained without conducting the complicated plane strain compression tests. Further studies are required to investigate quantitatively the difference between tensile and shear failures.

CONCLUSIONS

Three-point bending tests and plane strain compression tests were carried out to investigate the strain-softening behavior of cement-treated sand. The following conclusions were derived from the tests:

1. The bending test results were used to estimate the tension fracture energy G_f. The values of G_f for the cement-treated sand with an unconfined compression strength of around 1800 kPa ranged from 9 N/m to 12 N/m.
2. By employing the energy balance method proposed originally for concrete, the tension softening relations were evaluated based on the opening crack mouth displacements that were obtained from the bending tests. The tension-softening relations could be approximated by the 1/4 bi-linear model that was proposed originally for concrete.
3. In the plane strain compression tests, the strain localization zone that occurs during the strain-softening process was identified by the image analysis method. The stress-strain relationships in the shear failure zone were also obtained from the image analysis results. The shear-softening relations can be expressed approximately by an exponential function.
4. The shear failure zone in the specimen was observed with a microscope. The observation revealed that the shear band thickness of the cement-treated sand was approximately 3 times the mean size of the constituent sand particles.
5. The energy consumed per unit shear band area, G_{fs}, was estimated from the image analysis results. The value of G_{fs} ranged from 100 N/m to 180 N/m.
6. The difference in the energies consumed by the tensile and shear failures was discussed using an idealized model. This difference could be explained partially by the difference in the cementation areas that were broken in the failure zone.

ACKNOWLEDGEMENTS

The authors are grateful to Prof. K. Maekawa (the Department of Civil Engineering, the Univ. of Tokyo), for his kind suggestions during this study. The cooperation by Mr. T. Sato (IIS, the Univ. of Tokyo) is also appreciated.

REFERENCES

1) Alshibli, K. A. A. and Sture, S. (2000): Shear band formation in plane strain experiments of sand, *J. Geotech. Geoenviron. Engrg.*, ASCE, **126**(6), 495–503.
2) Ampadu, S. K. and Tatsuoka, F. (1993): Effects of setting method on the behavior of clays in triaxial compression from saturation to undrained shear, *Soils and Foundations*, **33**(2), 14–34.
3) Bažant, Z. P. (1989): Identification of strain-softening constitutive relation from uniaxial tests by series coupled model for localization, *Cement and Concrete Research*, **19**, 973–977.
4) Bažant, Z. P. and Oh, B. H. (1983): Crack band theory for fracture of concrete, *Materials and Structures*, **16**, 155–177.
5) Bažant, Z. P. and Xiang, Y. (1997): Size effect in compression fracture: splitting crack band propagation, *J. Engrg. Mech*, ASCE, **123**(2), 162–172.
6) Bhandari, A. R. and Inoue, J. (2005): Experimental study of strain rates effects on strain localization characteristics of soft rocks, *Soils and Foundations*, **45**(1), 125–140.
7) Desrues, J. and Viggiani, G. (2004): Strain localization in sand: an overview of the experimental results obtained in Grenoble using stereophotogrammetry, *Int. J. Numer. Anal. Meth. Geomech.*, **28**, 279–321.
8) Finno, R. J., Harris, W. W., Mooney, M. A. and Viggiani, G. (1997): Shear bands in plane strain compression of loose sand, *Géotechnique*, **47**(1), 149–165.
9) Goto, S., Tatsuoka, F., Shibuya, S., Kim, Y. S. and Sato, T. (1991): A simple gauge for local small strain measurements in the laboratory, *Soils and Foundations*, **31**(1), 169–180.
10) Han, C. and Drescher, A. (1993): Shear bands in biaxial tests on dry coarse sand, *Soils and Foundations*, **33**(1), 118–132.

11) Hayano, K., Maeshiro, T., Tatsuoka, F., Sato, T., Wang, L. and Kodaka, T. (1999): Shear banding in a sedimentary soft mudstone subjected to plane strain compression, *Geotech. Test. J.*, ASTM, **22**, 67–79.
12) Hillerborg, A. (1985): The theoretical basis of a method to determine the fracture energy G_F of concrete, *Materials and Structures*, **18**, 291–296.
13) Hillerborg, A., Modeer, M. and Petersson, P.-E. (1976): Analysis of crack formation and crack growth in concrete by means of fracture mechanics and finite elements, *Cement and Concrete Research*, **6**, 773–782.
14) Kobayashi, A. and Tatsuoka, F. (1982): Mechanical properties of saturated soft clay improved by cement-mixing V—Failure modes and strength properties—, *Seisan-Kenkyu*, IIS, University of Tokyo, **34**(10), 4–6 (in Japanese).
15) Koseki, J., Tatsuoka, F., Munaf, Y., Tateyama, M. and Kojima, K. (1998): A modified procedure to evaluate active earth pressure at high seismic loads, *Special Issue of Soils and Foundations*, 209–216.
16) Koseki, J., Salas-Monge, R. and Sato, T. (2005a): Plane strain compression tests on cement-treated sands, Geomechanics: Testing, Modeling, and Simulation, *Geotech. Special Publication*, ASCE, (143), 429–443.
17) Koseki, J., Sato, T. and Nishimoto, T. (2005b): Anisotropy in strength characteristics of cement-treated sand prepared by compaction, *Proc. Symp. Cement-treated Soils*, JGS, 365–368 (in Japanese).
18) Lade, P. V. (2003): Analysis and prediction of shear banding under 3D conditions in granular materials, *Soils and Foundations*, **43**(4), 161–172.
19) Li, V. C., Chan, C.-M. and Leung, C. K. Y. (1987): Experimental determination of the tension-softening relations for cementitious composites, *Cement and Concrete Research*, **17**, 441–452.
20) Murata, K., Nakano, M., Kimura, Y., Chimi, K., Tasaka, M., Inoue, A., Tatsuoka, F. and Yoshida, T. (1995): Stress-deformation relationships of shear band in PSC tests on cement-mixed sand, *Proc. Annu. Conf., JGS*, **30**, 729–732 (in Japanese).
21) Namikawa, T. (2006): Study on tensile and shear failure characteristics of cement-treated sand, *Doctor Thesis*, Univ. of Tokyo (in Japanese).
22) Namikawa, T. and Koseki, J. (2005): Post peak strain softening properties of cement-treated sand, *Proc. Symp. Cement-treated Soils*, JGS, 357–364 (in Japanese).
23) Namikawa, T. Suzuki, Y. and Koseki, J. (2005): Seismic response analysis of lattice-shaped ground improvement, *Deep Mixing 05*, 263–271.
24) Niwa, J., Sumranwanich, T. and Tangtermsirikul, S. (1998): New method to determine tension softening curve of concrete, *Proc. FRAMCOS-3*, 347–356.
25) Oda, M. and Kazama, H. (1998): Microstructure of shear bands and its relation to the mechanisms of dilatancy and failure of dense granular soils, *Géotechnique*, **48**(4), 465–481.
26) Oda, M., Takemura, T. and Takahashi, M. (2004): Microstructure in shear band observed by microfocus X-ray computed tomography, *Géotechnique*, **54**(8), 539–542.
27) Okuyama, Y., Yoshida, T., Tatsuoka, F., Koseki, J., Uchimura, T., Sato, N. and Oie, M. (2003): Shear banding characteristics of granular materials and particle size effects on the seismic stability of earth structures. *Proc. 3rd Int. Symp. Deformation Characteristics of Geomaterials, IS Lyon 03*, Balkema, 607–616.
28) Palmer, A. C. and Rice, J. R. (1973): The growth of slip surfaces in the progressive failure of over-consolidated clay, *Proc. Roy. Soc. Lond. A.*, **332**, 527–548.
29) Public Works Research Center (1999): *Technical Manual on Deep Mixing Method for Constructions on Land* (in Japanese).
30) RILEM Draft Recommendation (1985): Determination of the fracture energy of mortar and concrete by means of three-point bend tests on notched beams, *Materials and Structures*, **18**, 285–290.
31) Rokugo, K., Iwasa, M., Suzuki, T. and Koyanagi, W. (1989): Testing methods to determine tensile strain softening curve and fracture energy of concrete, *Fracture Toughness and Fracture Energy*, Balkema, 153–163.
32) Salas-Monge, R. (2002): Effects of large amplitude cyclic loading on deformation and strength properties of cement treated sand, *Master Thesis*, Univ. of Tokyo.
33) Salas-Monge, R., Koseki, J. and Sato, T. (2003): Cyclic plane strain compression tests on cement treated sand, *Bulletin of ERS, IIS, University of Tokyo*, **36**, 131–141.
34) Siddiquee, M. S. A., Tanaka, T., Tatsuoka, F., Tani, K. and Morimoto, T. (1999): Numerical simulation of bearing capacity characteristics of strip footing on sand, *Soils and Foundations*, **39**(4), 93–109.
35) Tatsuoka, F. and Kim, Y.-S. (1994): Deformation of shear zone in sedimentary soft rock observed in triaxial compression, *Localization and Bifurcation Theory for Soils and Rocks*, Balkema, 181–187.
36) Taylor, D. W. (1948): *Fundamentals of Soil Mechanics*, John Wiley and Sons, 329–361.
37) Uchida, Y., Rokugo, K. and Koyanagi, W. (1991): Determination of tension softening diagrams of concrete by means of bending tests, *J. Materials, Concrete Structures and Pavements of JSCE*, **426**(V-14), 203–212 (in Japanese).
38) Vardoulakis, I. and Goldscheider, M. (1981): Biaxial apparatus for testing shear bands in soils, *Proc. 10th Int. Conf. Soil Mech. Fund. Engrg. Stockholm*, Balkema, 819–824.
39) Vardoulakis, I. and Graf, B. (1985): Calibration of constitutive models for granular materials using data from biaxial experiments, *Géotechnique*, **35**(3), 299–317.
40) Vipulanandan, C., Ata, A. and Mebarkia, S. (1994): Fracture behavior of cement grouted sand, Fracture Mechanics Applied to Geotechnical Engineering, *Geotech. Special Publication*, ASCE, (43), 147–159.
41) Wittmann, F. H., Rokugo, K., Brühwiler, E., Mihashi, H. and Simonin, P. (1988): Fracture energy and strain softening of concrete as determined by means of compact tension specimens, *Materials and Structures*, **21**, 21–32.
42) Yoshida, T., Tatsuoka, F., Siddiquee, M. S. A., Kamegai, Y. and Park, C.-S. (1994): Shear banding in sands observed in plane strain compression, *Localization and Bifurcation Theory for Soils and Rocks*, Balkema, 165–179.